

In Vitro Experiments and Numerical Simulations of Airflow in Realistic Nasal Airway Geometry

CÉLINE CROCE,¹ REDOUANE FODIL,¹ MARC DURAND,^{2,3} GABRIELA SBIRLEA-APIOU,⁴
GEORGES CAILLIBOTTE,⁴ JEAN-FRANÇOIS PAPON,^{1,5} JEAN-ROBERT BLONDEAU,⁶
ANDRÉ COSTE,^{1,5} DANIEL ISABEY,¹ and BRUNO LOUIS¹

¹Fonctions Cellulaires et Moléculaires de l'Appareil Respiratoire et des Vaisseaux, Equipe Biomécanique Cellulaire et Respiratoire, INSERM UMR 651, Créteil, France; ²Laboratoire d'Anatomie, Faculté de Médecine de Saint-Etienne, France; ³Centre Hospitalier Emile Roux, Le Puy, France; ⁴Centre de Recherche Claude Delorme, Air Liquide, Jouy-en-Josas, France; ⁵Service d'ORL et de Chirurgie Cervico-Faciale, Centre Hospitalier Intercommunal de Créteil et Hôpital Henri Mondor (AP-HP), Créteil, France; and ⁶Service de Radiologie, Centre Hospitalier Inter-Communal de Créteil, Créteil, France

(Received 23 July 2005; accepted 21 February 2006; published online: 5 May 2006)

Abstract—Pressure–flow relationships measured in human plastinated specimen of both nasal cavities and maxillary sinuses were compared to those obtained by numerical airflow simulations in a numerical three-dimensional reconstruction issued from CT scans of the plastinated specimen. For experiments, flow rates up to 1500 ml/s were tested using three different gases: HeO₂, Air, and SF₆. Numerical inspiratory airflow simulations were performed for flow rates up to 353 ml/s in both the nostrils using a finite-volume-based method under steady-state conditions with CFD software using a laminar model. The good agreement between measured and numerically computed total pressure drops observed up to a flow rate of 250 ml/s is an important step to validate the ability of CFD software to describe flow in a physiologically realistic binasal model. The major total pressure drop was localized in the nasal valve region. Airflow was found to be predominant in the inferior median part of nasal cavities. Two main vortices were observed downstream from the nasal valve and toward the olfactory region. In the future, CFD software will be a useful tool for the clinician by providing a better understanding of the complexity of three-dimensional breathing flow in the nasal cavities allowing more appropriate management of the patient's symptoms.

Keywords—Nasal airway model, Nasal airflow, CT scans, Three-dimensional reconstruction, Computational fluid dynamics (CFD).

INTRODUCTION

Nasal airways play a very important role during respiration not only as the gateway to the respiratory tract but also as an air conditioner regulating temperature and humidity and cleaning inspired air.

Nasal cavities are two geometrically complex three-dimensional structures placed symmetrically on each side of the center of the face and separated by the nasal septum

(Fig. 1). During inspiration, air enters each nasal fossa by the “nostril” and then goes through a convergent funnel-shaped region called the “vestibule” leading to a constricted region called the “nasal valve.” Immediately after the nasal valve, the cross-sectional area of the airways increases appreciably as far as the region called “main nasal passage.” The lateral wall of the nasal cavities is irregular and carries bone plates covered with an erectile mucous membrane, which spread out before with the back of the nasal cavities, thus dividing respiratory flow. Their functions are to protect the entry of the sinuses, and increase the surface area of exchange for inspired air while maintaining the narrow shape of the cavity. Maxillary sinuses are cavities located within the facial bone, on each side of the nasal fossa with which they are in contact via an ostium of variable size (2–5 mm in internal diameter) and located in a space called the “middle meatus.” This middle meatus is the crossroads of the drainage openings of all anterior sinus cavities and plays a major pathophysiological role. The slit-shaped region above the middle turbinate between the nasal septum and the lateral wall of the main nasal passage is the superior meatus or olfactory airway. Nasal cavities are then connected to the rest of the respiratory tract by the nasopharynx.^{13,22} The airways therefore appear to be a highly complex system both geometrically and functionally, but the link between structure and function has not been fully elucidated, especially in the upper region.

For many years, several researchers have been interested in studying airflow in the nasal cavities. Early observations were made *in vivo*. Sullivan and Chang²⁸ used a novel method of anterior rhinomanometry in which an externally generated flow is passed through the nasal passage via a mouthpiece. They studied transnasal pressure–flow relationships for quasi-steady flows with different gases. According to these studies, the nasal passage behaves like

Address correspondence to Bruno Louis, INSERM U651, Faculté de Médecine, 8 rue du Général Sarrail, 94010, Créteil Cedex, France. Electronic mail: bruno.louis@creteil.inserm.fr

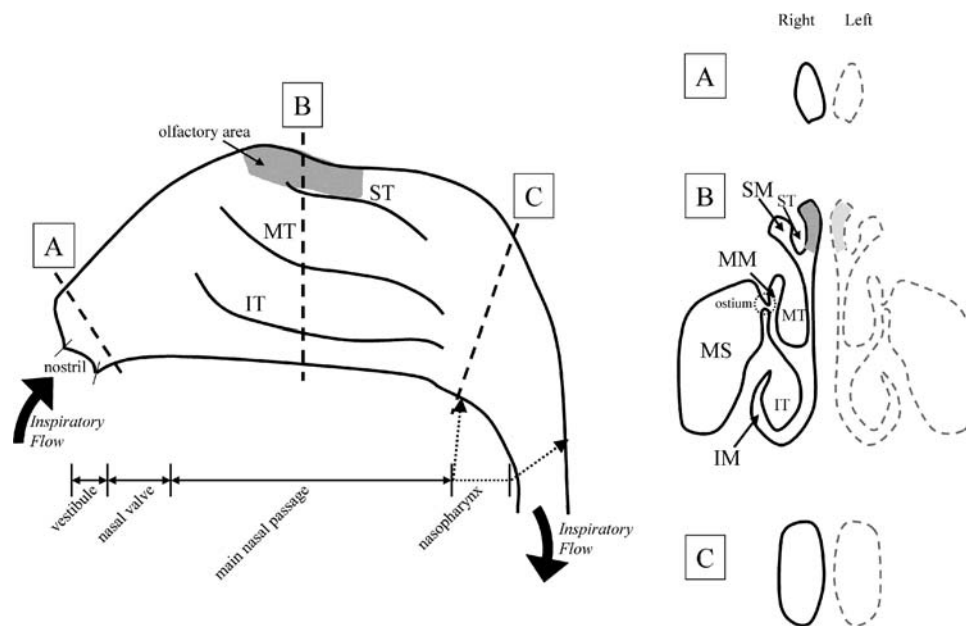


FIGURE 1. Schematization of a lateral view of a human right nasal cavity. On the right part of the figure, A, B, C correspond to three different nasal cross-sections represented on the lateral view shown on the left. IT, MT, and ST refer to inferior, middle, and superior turbinates. IM, MM, and SM refer to inferior, middle, and superior meatuses. MS refers to the maxillary sinus.

a rigid single duct with rough walls. For flow rates corresponding to quiet breathing, the flow was found to be transitional. According to these studies, the Reynolds number of the flow mainly determines nasal resistance. *In vivo* measurements have many limitations basically due to the complex three-dimensional anatomy and narrowness of nasal passages. To resolve this problem, some *in vitro* experimental studies were conducted with precise anatomical models of nasal cavities.^{7,8,11,21,25}

Schreck *et al.*²⁵ studied airflow in a threefold-enlarged plastic model of a left nasal cavity obtained from magnetic resonance images (4 mm apart). Flow visualization with water demonstrated the formation of two vortices behind the nasal valve: a larger vortex formed in the upper part of the cavity and a smaller vortex in the lower part of the cavity. Velocity measurements were obtained with a hot-wire anemometer and showed that most of the flow passed through the central part of the nasal cavity. Pressure drops were strongly influenced by nasal geometry. Hahn *et al.*⁸ studied flow patterns using a 20-fold-enlarged model of a right nasal cavity reconstructed from computed tomography scans (2 mm apart). The velocity profiles were obtained with a hot-wire anemometer and the intensity of turbulence was measured for flow rates corresponding to 180, 560, and 1100 ml/s in the real nose. They found that about 50% of the fluid flowed in the inferior part of the nasal cavity, while only 14% remained in the olfactory region at all flow rates studied. Flow was found to be laminar for flow rates less than 200 ml/s per nasal cavity. Kelly *et al.*¹⁴ used the particle image velocimetry (PIV) method to determine

two-dimensional instantaneous velocity vector fields for a steady flow rate of 125 ml/s in one nasal cavity. Their transparent silicone model of a human right nasal cavity was constructed from 26 computed tomography scans (CT scans) with a rapid prototyping technique. Flow was observed to be steady and laminar for the flow rate studied. They partitioned the nose into two regions, one for the highest velocities that contains the nasal valve and inferior part of the cavity, and the other for the lowest velocities that includes the olfactory area and the various nasal meatuses.

Many numerical studies on airflows in upper airways have been conducted since the 1990s, with the development of numerical simulation tools and progress in computers.^{2,12,15,19,26} For instance, Keyhani *et al.*¹⁵ created a finite-element mesh of a human nasal cavity obtained from axial CT scans (2 mm apart) of the experimental model used by Hahn *et al.*⁸ They numerically solved airflow through nasal airways with computational fluid dynamic (CFD) software, FIDAP[®] (Fluent Inc., Lebanon). Their results confirmed the laminar nature of flow for quiet breathing already found experimentally. For inspiratory flow, they found a maximal peak velocity on the nasal floor (under the inferior turbinate) and a lower peak in the middle of the airways (between the inferior and middle turbinates and the septum). According to this study, about 30% of inspiratory airflow passes below the inferior turbinate and about 10% passes in the olfactory area. It is noteworthy that most *in vitro* three-dimensional nasal models previously used in the literature are characterized by (i) a unique nasal cavity which, for example excludes a comparative approach between left and right

cavities, (ii) a variable but significant degree of idealization or smoothing imposed by the construction process specific to each nasal model which compromises the reliability of very local flow data and the study of their potential influence at the global level.

By contrast, in our study, we used a realistic model respecting nasal human airways including left and right nasal cavities and ostia that connect sinuses to upper airways. The physical model of nasal airways is obtained from a human plastinated head (i.e., after substituting polymers for water and lipids^{3,4}). The numerical model is obtained from the same physical model after scanning the plastinated head and a specific three-dimensional reconstruction procedure performed using the stack of CT images. In this study, we used in parallel a strictly similar physical nasal geometry and a numerical nasal geometry to validate spatial nose flow computation. In practice, we used longitudinal pressure–flow relationship measurements performed throughout the physical model as a first step to validate the numerical inspiratory flow calculations performed in the three-dimensional reconstructed geometry.

MATERIALS AND METHODS

Plastinated Nasal Airway Model

It is difficult to create an accurate model of nasal airways due to the complex anatomy of the nasal passages. We therefore chose to study a human plastinated specimen of nasal cavities and maxillary sinuses (Fig. 2) because

it constitutes the most realistic model.^{3,4} The anatomical specimen was obtained from a cadaver donated to the “Laboratoire d’Anatomie de la Faculté de Médecine Jacques Lisfranc (Saint-Etienne, France).” This type of donation is anonymous. Our plastinated model is the same as “model 2” used in the study by Durand *et al.*⁴ Plastination is a well-known technique for anatomical conservation. It consists of extracting water and lipids from biological tissues and then replacing them with curable polymers. The process includes fixation, dehydration, forced impregnation, and polymerization. The anatomical specimen is removed from a cadaver during the first 24 h after death and fixed in 10% formaldehyde. After fixation, the specimen is dehydrated by immersion in a cold acetone solution (-25°C). The dehydrated specimen is then immersed in silicone (S10 Biodur[®]) and placed in a freeze drier for impregnation under low vacuum. The geometry of the plastinated head can be seen as a basic state for the nasal geometry. Indeed, this technique allows to preserve most of the nasal airway anatomy, but after removal of most of vascular blood irrigation due to post-mortem condition. The plastination process keeps the three-dimensional complexity of the nasal geometry in the context of decreasing the thickness of the mucous membrane of the turbinates. Indeed, according to von Hagens *et al.*²⁹ one can admit a 10% retraction of tissues after the process of plastination. Due to the cadaver decongestion, dehydration, forced impregnation, and polymerization, we expect that the plastinated nose behaves like the nose of a patient after mucosal decongestion. The realistic character of the

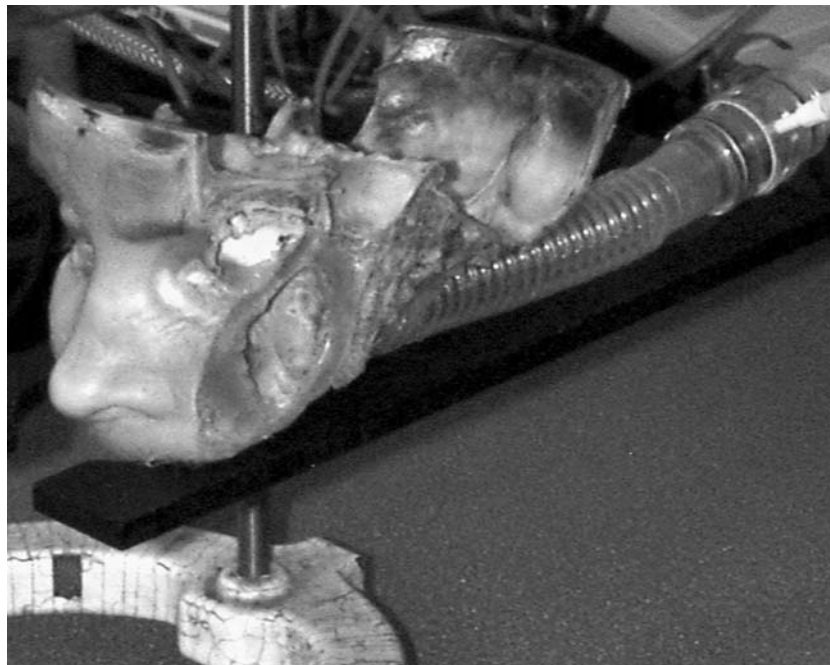


FIGURE 2. Photograph of the plastinated head connected by a tube to the negative pressure generator.

TABLE 1. Thermodynamic characteristics of the three gases used.

| | HeO ₂ | Air | SF ₆ |
|---------------------------------|------------------|-------|-----------------|
| ρ ($\times 10^{-6}$ Pa s) | 0.57 | 1.225 | 5.99 |
| η (kg/m ³) | 21.7 | 18.1 | 15.0 |

Note. HeO₂: (65%He + 35%O₂); ρ : Density; η : Dynamic viscosity.

nasal airway model has been previously validated by CT scan.⁴

Experimental Measurement Protocol and Set-up

Considering the difficulty to determine a representative hydraulic diameter in such a complex geometry, we found useful to test the validity of a “general law of the pressure–flow relationships” by using different gases, i.e., by changing the physical properties of the gas. Three different gases were used for this study: Heliox (gas mixture containing 65% He and 35% O₂), room air, and SF₆ (sulfur hexafluoride). The thermodynamic properties of these gases are indicated in Table 1. Inspiratory flows for the three different gases were generated by a negative pressure generator made of a turbine rotating at a constant adjustable speed, which was connected to the nasopharyngeal extremity of the plastinated airway model. A compressed air source replacing the turbine generated expiratory airflows. For measurements with air, the model was fixed to a tripod directly in contact with atmospheric pressure (see Fig. 2). For the other two gases, the model was placed in a hermetically sealed Plexiglas box connected upstream to a 100-liter balloon constituting a uniform atmosphere of the test gases (Heliox or SF₆). Before measurements, the two open cavities (corresponding to the maxillary sinuses, see Fig. 2) on the lateral sides of the head were sealed using two plates to mimic the physiological conditions in which sinuses are closed systems only open to the upper airways through the ostia.

Steady flow was measured with a Fleisch pneumotachograph (Lausanne, Switzerland) coupled to a differential pressure transducer (Validyne DP45, Northridge, CA) by short tubes. The turbine simulating inspiration was connected to a potentiometer (DEREIX, S.A., Paris, Rotofransfo) allowing control the flow rate of the output gas. During expiration, various flow rate values were obtained by driving the compressed air tap with a valve. This set-up allowed us to investigate flow rates ranging from 10 to 1500 ml/s. The pneumotachograph was calibrated for each gas by integrating the signal resulting from several successive fillings and drainings from a 1-liter syringe. The static pressure drop between the extremities of the model (ΔP_{static}) was measured with a differential pressure transducer (Validyne DP45, Northridge, CA). All signals were

digitized at 128 Hz using an analog-digital system (MP100, Biopac System).

Three-dimensional Model Reconstruction and Numerical Flow Computation

The three-dimensional computational geometry used for this numerical study was derived from CT scan images of the plastinated head. The scans provided 196 contiguous axial images (0.5 mm apart). The stack of CT images in DICOM format was imported into a commercial software package: AMIRA[®] (Mercury Computer System, Berlin). Construction of this type of geometric model first requires a segmentation step carried out interactively to isolate the desired region of interest. Segmentation assigns to each pixel of the image a label describing to which region or material the pixel belongs, e.g., exterior or interior. Segmentation is a prerequisite for surface model generation. The segmentation threshold must be chosen with care, as, depending on the choice of this threshold, some sinus cavities could be absent from the three-dimensional reconstruction because the diameter of the ostium that connects the sinus to the main nasal passage was too small to be detected. To overcome this difficulty, an experienced ENT surgeon read the nasal CT scans in order to select a correct segmentation threshold. We then used AMIRA[®] software to successively construct a triangular surface and an unstructured volumetric tetrahedral grid of the segmented object. During the two-dimensional segmentation of the data from the plastinated head CT scans, we did not encounter major problems for the choice of the segmentation threshold. Indeed, from comparison with images issued from *in vivo* subject, the plastination process makes that the specimen not to have mucus on its walls. So, the contrast in the two-dimensional images between air and solid plastinated tissues is clearer than in the case of images issued from *in vivo* subjects. Moreover, the plastinated head is rigid, so there is no risk of artifacts due to a movement of the patient during the scan or to dental leadings. The original mesh, Amira normal mesh (A-NM), was composed of 100,004 triangular faces for the surface grid and 825,239 tetrahedral cells for the volumetric grid (Fig. 3). A preliminary inspiratory airflow simulation was performed with this A-NM. The result of this first simulation was used to adapt the mesh via the CFD software in order to resolve large pressure gradients in the flow field. This adapted mesh (F-AM) consisted of 1,353,795 tetrahedral cells. The quality of the mesh was estimated by the triangle aspect ratio (<10) and tetra aspect ratio (<10), as regularly reported in the literature.¹⁵

Numerical simulations of three-dimensional inspiratory airflows were performed in the three-dimensional reconstructed model derived from the plastinated nose. For our simulations, flows were supposed to be incompressible, quasi-steady, and laminar. Previous studies have shown that

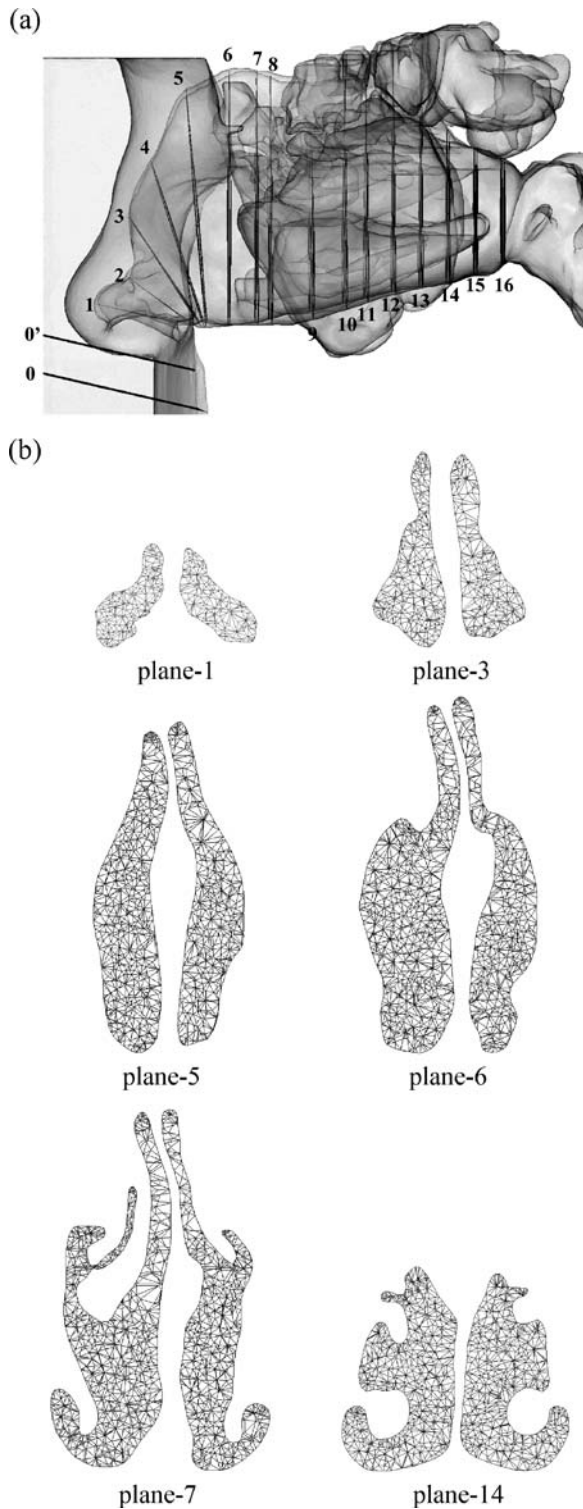


FIGURE 3. (a) Lateral transparent view of the three-dimensional reconstructed nasal cavities. (b) Cross-sections of the finite-volume mesh before mesh-adaptation by the CFD software (A-NM composed of 825,239 tetrahedral cells).

flow remained laminar as long as the flow rate in one nostril was less than 200 ml/s.^{8,11,25} Flow rates expressed in this study correspond to inspiratory flows up to 353 ml/s through both nasal cavities. Governing equations for momentum and mass conservation were solved by a commercial CFD software package, FLUENT[®] (Fluent Inc., Lebanon), using a control-volume-based method. The solution algorithm used was a segregated solver. The governing equations were linearized with an implicit method. A pressure difference between the inlet and outlet of the model was applied as boundary condition. At the nose entry, the pressure was set to zero (atmospheric pressure), and a negative pressure was set at the outlet of the model, in order to simulate an inspiratory flow. A no-slip condition at the walls was assumed. The boundary conditions were applied in the CFD procedure by introducing two additional volumes. The first was situated in front of the nose and the second at the outlet of the model. The first is a kind of box ($\sim 150 \text{ cm}^3$) so that entry of the nostrils was in contact with a uniform atmosphere of gas. The second is a virtual duct added to the grooved tube connected to the nasopharynx (length = $6 \times$ diameter) in order to move away the boundary.

RESULTS

Experimental Measurements

The classical Moody diagram described pressure–flow measurement data, i.e., by plotting the normalized total pressure loss versus the Reynolds number of the flow. The normalized total pressure loss is defined by $\frac{\Delta P_{\text{total}}}{\frac{1}{2}\rho\bar{u}^2}$ where ρ is the density and \bar{u} the mean velocity computed in the tube at the outlet of the model ($D_{\text{tube}} \approx 2.48 \text{ cm}$). The Reynolds number was also defined from the diameter of the tube at the outlet of the model: $Re_{\text{tube}} = \frac{\bar{u} \times D_{\text{tube}}}{\nu}$ where ν is the kinematic viscosity. Figure 4 presents these results in air for expiratory and inspiratory flows in each nostril (left or right) and when the gas passes through both the nostrils. Inspiratory and expiratory flows appear to describe identical curves. The curves corresponding to the three nostril conditions are clearly distinct, but conserve the same shape. For these three conditions, the slope of the curves seems to be close to -1 at very low flow rates ($Re_{\text{tube}} < 70$) and gradually reaches -0.33 with increasing values of Reynolds number. Figure 5 presents the results for the three gases tested in inspiratory flows when the flow passes through both the nostrils. Interestingly, the curves for the three gases collapse into a single curve when plotted on this non-dimensional diagram.

Experimental Versus Numerical Results

Comparisons between experimental and numerical inspiratory data were inferred by plotting on the same graph the measured and simulated pressure drops obtained when the gas was passing through both the nostrils in

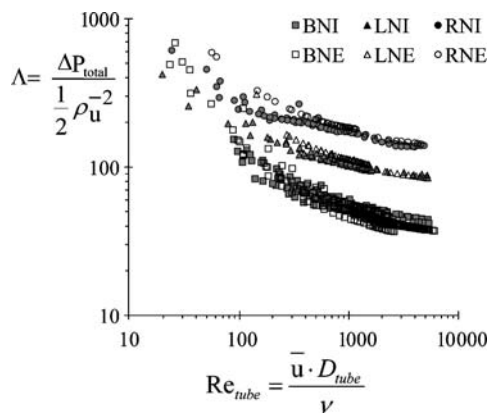


FIGURE 4. Moody diagram of the adimensional measured total pressure drop, Λ , vs. the adimensional flow rate, Re_{tube} . The data were plotted in air for inspiratory and expiratory flows in each nostril (left and right) and when the gas was passed through both the nostrils. *Solid symbols* represent inspiratory flow. *Empty symbols* represent expiratory flow. *Circular symbols* represent the right nostril (RN). *Triangular symbols* represent the left nostril (LN). *Square symbols* represent the gas passing through both the nostrils (BN).

adimensional (Fig. 6) form. Simulations and experiments showed a good agreement except for the highest values of flow rates (flow rate ≥ 272 ml/s or $Re_{tube} \geq 959$). Nevertheless, the disagreement for the highest value simulated (353 ml/s) was less than 17%.

Numerical Pressure Drop and Flow Distribution

CFD computation allows to infer the mean total pressure in any section of the model. Figure 7 presents this pressure

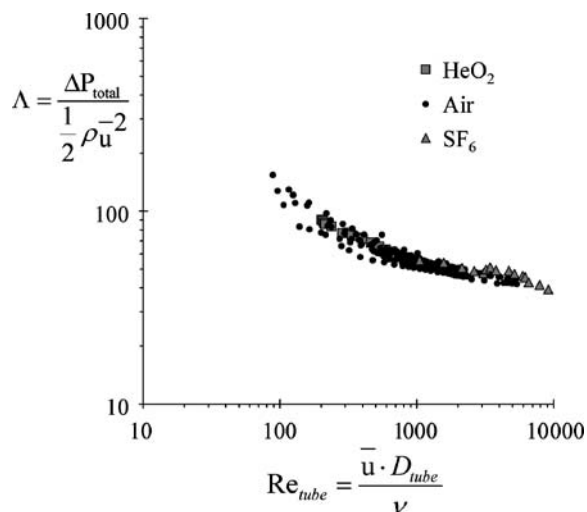


FIGURE 5. Moody diagram of the adimensional measured pressure drop, Λ , vs. the adimensional flow rate, Re_{tube} . The data were plotted in inspiratory flow for three respiratory gases (Air, 65%He–35%O₂, and SF₆) when the gas was passed through both the nostrils.

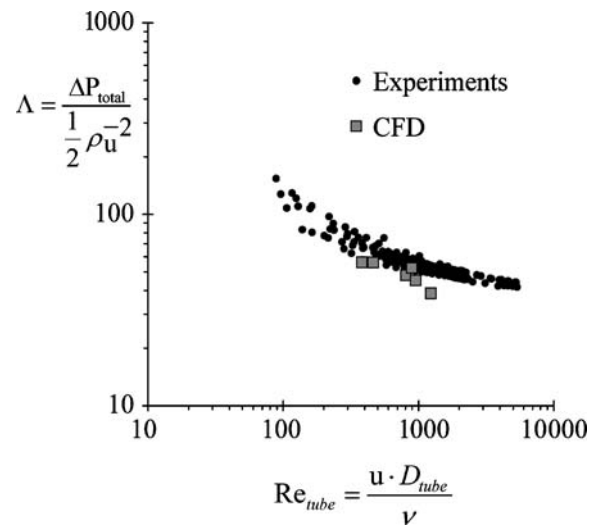


FIGURE 6. Comparison of the total pressure drop measured in air when the gas was passed through both the nostrils in inspiratory flow with the computational fluid dynamics results. The total pressure drop vs. flow rate is plotted in adimensional form.

for both the nostrils for different sections [Fig. 3(a)] of the model when the inspiratory flow is passing through both the nostrils. The different sections were chosen in order to follow the “natural” central axis of each nostril. The distance axis in Fig. 7 is the curvilinear axis through the center of gravity of each section. We observed that the right nostril induced more negative pressure than the left nostril. This difference was associated with a larger value of flow rate on the left side than on the right side. Figure 8 presents the corresponding flow velocity distribution in some of these sections for a medium flow rate of 231 ml/s. Results showed that predominant flow was in the inferior part of the nasal cavities, under the middle turbinate, through the middle and inferior meatuses. The highest velocities were in the nasal valve region and the lowest velocities were in the upper part (olfactory region). For this same flow rate, we also inferred by CFD the three-dimensional-streamlines colored for velocity magnitude (Fig. 9). Two vortices are visible in this figure. The larger vortex is localized in the upper part of the nasal cavities and reaches very low velocities. The second, less evident vortex is localized posterior to the nasal valve in front of the inferior turbinate head.

DISCUSSION

The main finding of this study is the good agreement observed between CFD simulations and experimental measurements for inspiratory flow rates below 250 ml/s (see Fig. 6). These results confirm the ability of CFD software to describe nasal flows, with their associated pressure drops, in a physiologically realistic physical model of the nasal airways. Our physical model as its three-dimensional

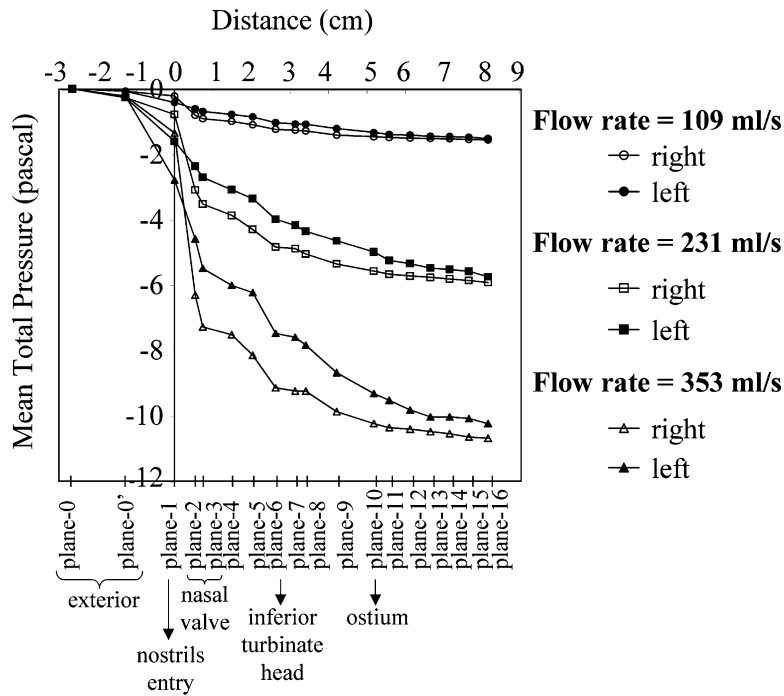


FIGURE 7. Mean total pressure in different sections of the nasal model. These mean pressures are plotted vs. the abscissa of the center of gravity of each section (see text). These pressures are computed by CFD for three distinct flow rates (109, 231, and 353 ml/s) and for each nostril when the flow is an inspiratory flow going through both the nostrils.

reconstruction reproduces most of the physiological features characterizing a human nose and includes both left and right nasal cavities. By comparison, the three-dimensional reconstructions found in the literature in realistic models used slices spaced 1 or 3 mm apart^{2,15,16,27} that necessarily introduces some degree of idealization. Indeed, in small and thin regions (e.g., the ostium connecting the main nasal passage to the sinuses and whose internal diameter does not exceed 2–5 mm) or in regions of the nasal cavities where there are abrupt changes in the shape of the airway (e.g., the vestibule or the turbinate heads), a three-dimensional reconstruction made from CT scan images too spaced could prevent the capturing of the anatomical features in detail. The study of dynamic flow conditions (to cover the variety of physiological conditions) including, e.g., the velocity and the pressure in the very local regions of physiological interest could be affected by this lack of anatomical details.

In this work, we use the acoustic reflection method in order to evaluate the resulting geometry of the plastinated nose. The longitudinal area profile of the nasal cavity was obtained by the two-microphone acoustic reflection method.^{17,18} It permitted to obtain the cross-sectional areas of the nasal airway as a function of the distance along the longitudinal axis, with a spatial step increment of $\Delta L \approx 0.41$ cm. Cross-sectional areas are the mean result of 10 repeated acquisitions. The coefficients of variation (standard deviation/mean) were found to be less than 2%. We found that the cross-sectional areas of this plastinated

nose model are in the range of the areas of healthy patients with mucosal decongestion obtained by acoustic reflection method.²⁰

It is hard to pinpoint the exact reason for the relative disagreement observed at the highest values of flow rates between experimental and numerical results except that laminar flow may not be verified throughout the model. Consequently, it was more difficult to achieve convergence for the highest flow rate values. The CFD model used to compute inspiratory airflows was the laminar model. This choice was based on the Reynolds number computed in the tube at the outlet of the model ($Re_{\text{tube}} < 1250$). This Reynolds number is calculated in a relatively large section of the model. Computed in a narrower section, the Reynolds number would have been higher and the laminar model in this locus would have become questionable, and could possibly explain the underestimation made by the CFD results. The Moody diagram, in which the slopes are identical for the three gases (Fig. 5) and in which these slopes decrease from -1 at the lowest values of flow rates, to -0.33 for the highest values of flow rates (see Figs. 4 and 5), appears to be in favor of this assumption. Indeed, these slopes do not reach the Blasius law slope (-0.25), i.e., for a hydraulically smooth turbulent flow, but become close at the high flow rates tested. Further studies are required to explore the choice of the CFD model in flow conditions in which some flow regions are conditionally turbulent (in this case above 250 ml/s, i.e., for a flow rate above 125 ml/s per nostril). This

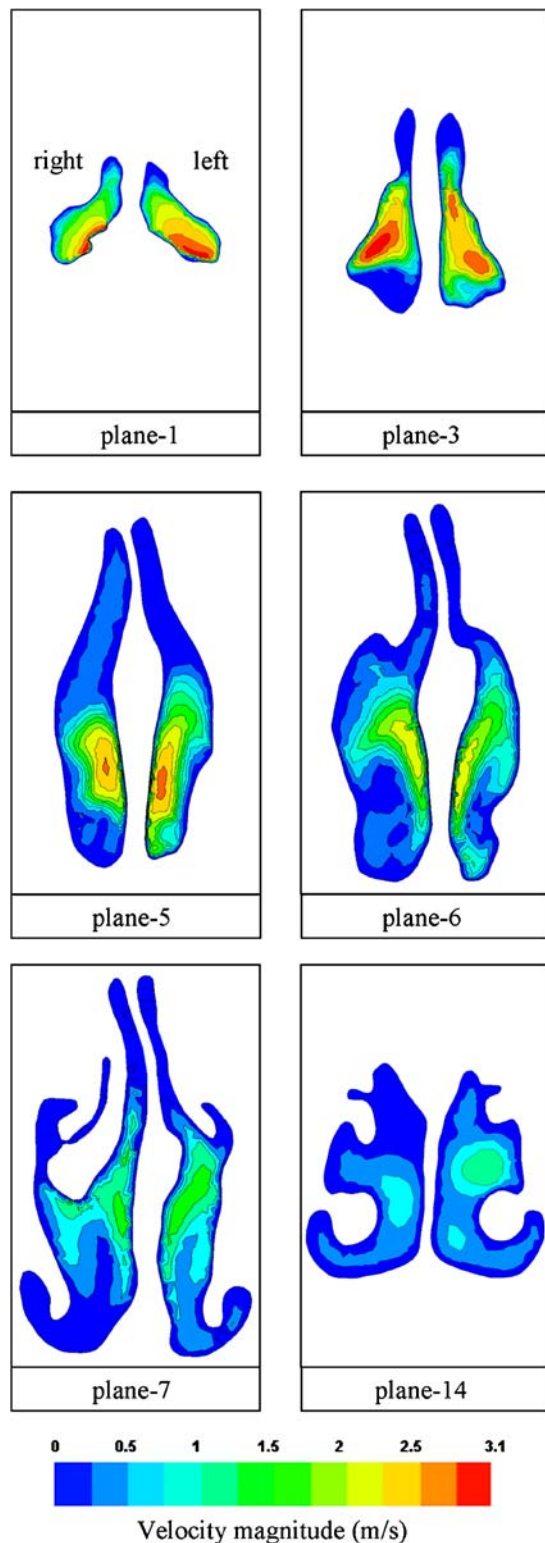


FIGURE 8. Velocity field in some sections of the human nasal model for a medium inspiratory flow rate of 231 ml/s. The velocity field is colored for velocity magnitude. The corresponding sections are indicated in Fig. 3(a). These sections more or less correspond to the nostril entry (plane-1), the end of the valve region (plane-3), the head of the inferior turbinate (plane-6 and plane-7), and the tails of the turbinates (plane-14).

laminar-to-turbulent transition value seems slightly smaller than the one (200 ml/s) indicated in the literature.^{8,11,25} This difference is difficult to explain. Nevertheless, we can note that our three-dimensional reconstruction based on CT scans used axial slices taken 0.5 mm apart allowing very precise reconstruction, while these authors^{8,11,25} used physical models reconstructed from CT scans with slices spaced 2 or 4 mm apart. Such a large increment between slices induces some degree of smoothing that can increase in the numerical simulation the laminar-to-turbulent transition value in terms of Reynolds number and/or flow rate. This last explanation suggests that the geometrical accuracy of the nasal airway model is especially important for flow rate above 250 ml/s, i.e., for any breathing more important than a quiet normal breathing like, for example, the one encountered during hyperventilation.

Velocities observed in our study are in agreement with the results of the literature^{2,8,11,15,27} both in terms of value and in terms of position. For example, the maximum velocity found in this study was about 3.1 m/s (in the valve region for a flow rate of 231 ml/s), while Keyhani *et al.*¹⁵ reported a value of 4 m/s (at the end of the nasal valve in an uninasal model for a flow rate of 125 ml/s) and Subramaniam *et al.*²⁷ reported a value of 4.2 m/s (in the posterior segment of the nasal valve for a flow rate of 250 ml/s). Our values are slightly lower but the present model has slightly larger areas (data not shown). The anterior part of the nose behaves like a convergent–divergent tube. During inspiration, air entering the nostrils undergoes a sudden acceleration due to nasal valve narrowing and then a slow deceleration when entering the vestibule. The velocity decreases considerably downstream from the nasal valve region due to the sudden expansion of the cross-sectional area posterior to the nasal valve (data not shown) especially in the vertical planes of the nose. This phenomenon is not as marked for the more or less idealized models encountered in the literature. The width of passages in the main nasal airways is greater than that of the model studied by Hahn *et al.*⁸ The differences in the above peak velocities, measured at the central portions of the airway, could be due to variations in the shape of the nasal passages of two different models. These variations are probably due to inter-individual anatomical differences.

Narrowing of the nasal valve area associated with the change in direction of flow at the passage from the entry of the nostrils to the vestibule generates the vortices observed in the olfactory region and in the lower part of the cavities before the head of the inferior turbinate.^{12,21,25,27,30} The vortex in the olfactory region is associated with very low velocities (0.4 m/s, at a flow rate of 231 ml/s). It confirms the physiological concept that the olfactory sensing organ requires sufficiently long resident times for olfactory molecules (present at very low concentrations) to bind to the neuroepithelium. The second vortex in front of the head of the inferior turbinate seems to initiate a flow separation. The main part of the flow goes between the

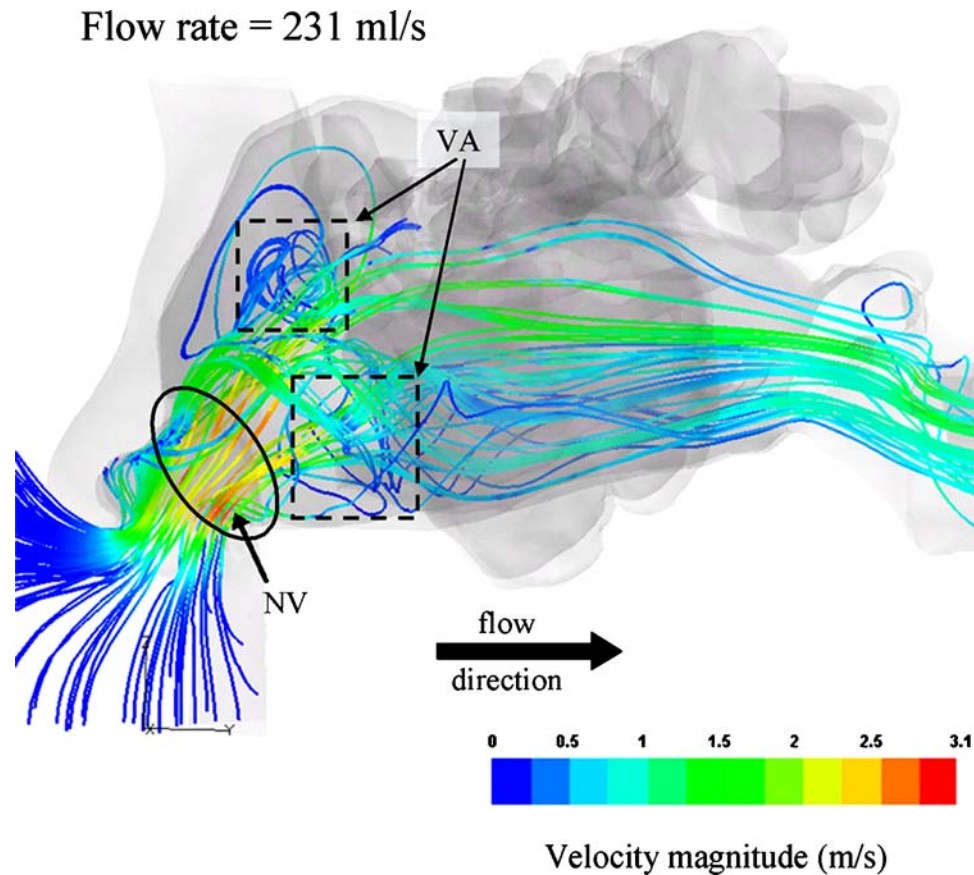


FIGURE 9. Three-dimensional-streamlines colored for velocity magnitude for a medium inspiratory flow rate of 231 ml/s. The nasal valve (NV) region is circled and indicated by an arrow. The two main regions of vortices are located in the two square frames indicated by arrows (VA: vortex area).

inferior and middle turbinates (see Fig. 8, planes 6–7–14); the velocities of the flow under the inferior turbinate and above the middle turbinate are very small. This last result was confirmed by previous experimental and computational studies.^{5,15,23}

In our work, we have tested the validity of the CFD computation by comparing the pressure–flow relationships measured and estimated by CFD. It is clear that a correct estimation of the pressure drop by CFD does not justify that all local details of the flow are well described by CFD. Nevertheless, due to the fact the pressure drop is the result of the integrated velocity gradient along the entire model, we can reasonably assume that a large part of the velocity gradients should be correctly estimated by CFD especially in the boundary layers where the most important part for the pressure drop occurs. By contrast, it is much less evident that the pressure drop validates the vortices. Fortunately for us the description of the vortices that we found with the CFD software agrees with the previous findings and most particularly the experimental study of Schreck *et al.*²⁵ So, we feel quite confident with the CFD results presently obtained in our study.

From the Moody diagram we found that inspiratory and expiratory data describe almost identical curves (Fig. 4). This has already been observed *in vivo*²⁸ and seems to indicate that entry effects do not play a significant role in the pressure drop throughout the nasal cavity. Our results indicate that the main total pressure drop arises in the anterior part of the nose (Fig. 7). 92% of the total pressure drop is generated between the nostril and the ostium (between planes 0 and 10). This result is in agreement with the physiological observations made *in vivo* by Hirschberg *et al.*,¹⁰ who found that the anterior part of a normal nose predominates in nasal resistance. In this study, we observed that about 48% of the total pressure drop is reached in the nasal valve region (plane-2), i.e., 0.54 cm after the nostril (~7% of the nasal cavity length). Moreover, 76% of the total pressure drop was reached at the level of the turbinate (plane-6 and after). From a physiological point of view, these last results are interesting, as clinicians have reported inspiratory flow limitations in the nose since the 1970s.^{1,24} This phenomenon can be explained by collapse of the nasal valve due to wall compliance (not represented with this model), which induces an increase in pressure drop. Our

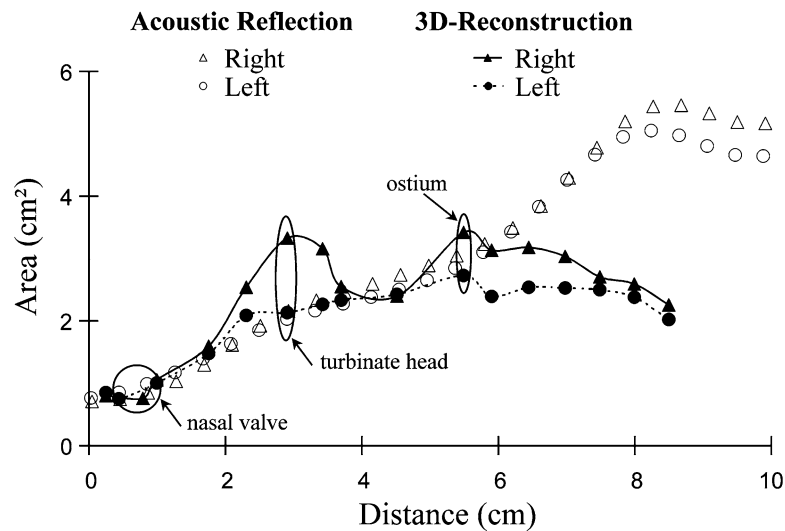


FIGURE 10. Comparison between the cross-sectional areas inferred by acoustic reflection method (*empty symbols*) and the cross-sectional areas obtained after three-dimensional reconstruction (*solid symbols*). The distance abscissa is the position of the center of gravity of each section for the three-dimensional reconstruction and the position along the curvilinear longitudinal axis of the cross-sectional area for the acoustic reflection method.

results show that this pressure drop under baseline conditions already reaches 76% at the turbinate and only 48% at the valve, suggesting that collapse may be more marked in the deeper regions, as recently suggested by Fodil *et al.*⁶ We did not observe the same pressure drop in the left and right nasal cavities. This dissymmetry, clearly observed in the Moody diagram (Fig. 4), between the two nostrils was already observed by the clinical investigation of the model that detected a *concha bullosa* (common “anatomic variant” characterized by pneumatized middle turbinate) in the right nasal cavity.

The “natural” central axis, i.e., the choice of the various planes [Fig. 3(a)], may be considered as purely arbitrary. Nevertheless, comparison of the areas obtained by acoustic reflection and the areas obtained after the three-dimensional reconstruction (Fig. 10) provide a relatively good agreement as far as plane-10. The ostium is included in this plane. It is well-known that the acoustic method tends to overestimate the area lying beyond the ostium due to the artifact induced by the paranasal sinuses,⁹ as part of the acoustic wave would be transmitted in the sinuses via the ostia, which would introduce overestimation of the inferred area. The acoustic reflection method gives the cross-sectional areas versus the curvilinear abscissa of these cross-sectional areas. With this type of geometry, it is nearly impossible to determine from the three-dimensional reconstruction the axis following the cross-sectional areas along the nasal cavity. To define our “natural” axis, we therefore started with a more or less horizontal plane at the entry of the nostrils that we gradually rotated and translated in the direction of the nasal cavity to reach the vertical planes of the median part of the nasal cavity [see Fig. 3(a)].

The relatively good agreement between acoustic data and three-dimensional reconstruction data in the anterior part of the nose seems to indicate that this arbitrary choice more or less corresponded to the cross-sectional area axis.

In summary, this study is an important step to validate the ability of CFD software to describe pressure drop and flow, in a physical model respecting the reality of the nasal airways geometry. During inspiration, the nose behaves like a convergent–divergent tube and generates a vortex with low velocities in the olfactory zone. The flow can be divided into two parts. A first part of the flow with relatively high velocity values passes through the lower half of the nasal cavities and seems therefore devoted to respiration, while a second part of the flow with much lower velocity values passes through the higher half of the nasal cavities and is probably devoted to olfactory function. In the future, CFD may represent a useful tool for the engineers to relate micro-to macro-phenomena and also for the clinicians to obtain a more accurate diagnosis or to predict the functional effect of treatment. At present, the method of investigation used in routine practice provides limited information about nasal function. For example, CFD would allow more accurate definition of the zones in which highly negative pressures increase the risk of collapse. It could also be used to predict the functional effect of a treatment such as surgery designed to enlarge the nasal fossa (flow and pressure).

ACKNOWLEDGMENTS

This study was part of a collaborative project entitled R-MOD and supported by grants from Air Liquide and the French Ministry of Research.

References

- ¹Bridger, G. P., and D. F. Proctor. Maximum nasal inspiratory flow and nasal resistance. *Ann. Otol. Rhinol. Laryngol.* 79:481–488, 1970.
- ²Castro, F., P. Castro, A. Delgado, C. Méndez, and C. Cenfor. Computational fluid dynamics simulations of the airflow in the human nasal cavity. In: Proceedings of the 7th International Symposium on Fluid Control, Measurement and Visualization, 2003.
- ³Durand, M. Réalisation et validation d'un modèle plastiné des cavités nasosinusiennes pour l'étude de la diffusion des aérosols. Saint-Étienne: DEA de Génie Biologique et Médical, 1999.
- ⁴Durand, M., P. Rusch, D. Granjon, G. Chantrel, J. M. Prades, F. Dubois, D. Esteve, J. F. Pouget, and C. Martin. Preliminary study of the deposition of aerosol in the maxillary sinuses using a plastinated model. *J. Aerosol. Med.* 14:83–93, 2001.
- ⁵Elad, D., R. Liebenthal, B. L. Wenig, and S. Einav. Analysis of air flow patterns in the human nose. *Med. Biol. Eng. Comput.* 31:585–592, 1993.
- ⁶Fodil, R., L. Brugel-Ribere, C. Croce, G. Sbirlea-Apiou, C. Larger, J. F. Papon, C. Delclaux, A. Coste, D. Isabey, and B. Louis. Inspiratory flow in the nose: A model coupling flow and vasoerectile tissue distensibility. *J. Appl. Physiol.* 98:288–295, 2005.
- ⁷Girardin, M., E. Bilgen, and P. Arbour. Experimental study of velocity fields in a human nasal fossa by laser anemometry. *Ann. Otol. Rhinol. Laryngol.* 92:231–236, 1983.
- ⁸Hahn, I., P. W. Scherer, and M. M. Mozell. Velocity profiles measured for airflow through a large-scale model of the human nasal cavity. *J. Appl. Physiol.* 75:2273–2287, 1993.
- ⁹Hilberg, O., and O. F. Pedersen. Acoustic rhinometry: Influence of paranasal sinuses. *J. Appl. Physiol.* 80:1589–1594, 1996.
- ¹⁰Hirschberg, A., R. Roithmann, S. Parikh, H. Miljeteig, and P. Cole. The airflow resistance profile of healthy nasal cavities. *Rhinology* 33:10–13, 1995.
- ¹¹Hopkins, L. M., J. T. Kelly, A. S. Wexler, and A. K. Prasad. Particle image velocimetry measurements in complex geometries. *Exp. Fluids* 29:91–95, 2000.
- ¹²Hörschler, I., M. Meinke, and W. Schröder. Numerical simulation of the flow field in a model of the nasal cavity. *Comput. Fluids* 32:39–45, 2003.
- ¹³Jones, N. The nose and paranasal sinuses physiology and anatomy. *Adv. Drug Deliv. Rev.* 51:5–19, 2001.
- ¹⁴Kelly, J. T., A. K. Prasad, and A. S. Wexler. Detailed flow patterns in the nasal cavity. *J. Appl. Physiol.* 89:323–337, 2000.
- ¹⁵Keyhani, K., P. W. Scherer, and M. M. Mozell. Numerical simulation of airflow in the human nasal cavity. *J. Biomech. Eng.* 117:429–441, 1995.
- ¹⁶Lindemann, J., T. Keck, K. M. Wiesmiller, G. Rettinger, H. J. Brambs, and D. Pless. Numerical simulation of intranasal air flow and temperature after resection of the turbinates. *Rhinology* 43:24–28, 2005.
- ¹⁷Louis, B., R. Fodil, S. Jaber, J. Pigeot, P.-H. Jarreau, F. Lofaso, and D. Isabey. Dual assessment of airway area profile and respiratory input impedance from a single transient wave. *J. Appl. Physiol.* 90:630–637, 2001.
- ¹⁸Louis, B., G. Glass, B. Kresen, and J. Fredberg. Airway area by acoustic reflection: the two-microphone method. *J. Biomech. Eng.* 115:278–285, 1993.
- ¹⁹Naftali, S., M. Rosenfeld, M. Wolf, and D. Elad. The air-conditioning capacity of the human nose. *Ann. Biomed. Eng.* 33:545–553, 2005.
- ²⁰Papon, J. F., L. Brugel-Ribere, R. Fodil, C. Croce, C. Larger, M. Rugina, A. Coste, D. Isabey, F. Zerah-Lancner, and B. Louis. Nasal wall compliance in vasomotor rhinitis. *J. Appl. Physiol.* doi:10.1152/japplphysiol.00575.2005, 2005.
- ²¹Park, K. I., C. Brücker, and W. Limberg. Experimental study of velocity fields in a model of human nasal cavity by DPIV. Laser anemometry, advances and applications. In: Proceeding of the 7th International Conference, Germany, September 8–11, 1997.
- ²²Proctor, D. F. Physiology of the upper airway. In: Handbook of Physiology. Respiration I, edited by W. O. Fenn and H. Rahn. Washington, DC: American Physiological Society, 1964, pp. 309–345.
- ²³Proctor, D. F. Airborne disease and the upper respiratory tract. *Bacteriol. Rev.* 30:498–513, 1966.
- ²⁴Proctor, D. F. The upper airways. I. Nasal physiology and defense of the lungs. *Am. Rev. Respir. Dis.* 115:97–129, 1977.
- ²⁵Schreck, S., K. J. Sullivan, C. M. Ho, and H. K. Chang. Correlations between flow resistance and geometry in a model of the human nose. *J. Appl. Physiol.* 75:1767–1775, 1993.
- ²⁶Simmen, D., J. L. Scherrer, K. Moe, and B. Heinz. A dynamic and direct visualization model for the study of nasal airflow. *Arch. Otolaryngol. Head Neck Surg.* 125:1015–1021, 1999.
- ²⁷Subramaniam, R. P., R. B. Richardson, K. T. Morgan, J. S. Kimbell, and R. A. Guilmette. Computational fluid dynamics simulations of inspiratory airflow in the human nose and nasopharynx. *Inhal. Toxicol.* 10:91–120, 1998.
- ²⁸Sullivan, K. J., and H. K. Chang. Steady and oscillatory transnasal pressure–flow relationships in healthy adults. *J. Appl. Physiol.* 71:983–992, 1991.
- ²⁹von Hagens, G., K. Tiedemann, and W. Kriz. The current potential of plastination. *Anat. Embryol. (Berl.)* 175:411–421, 1987.
- ³⁰Weinhold, I., and G. Mlynski. Numerical simulation of airflow in the human nose. *Eur. Arch. Otorhinolaryngol.* 261:452–455, 2004.